Defect-Mediated Conductivity Enhancements in Na$_{3-x}$Pn$_{1-x}$W$_x$S$_4$ (Pn = P, Sb) using Aliovalent Substitutions

Till Fuchs[a,b], Sean P. Culver[a,b], Paul Till[a,b], Wolfgang G. Zeier*[a,b]

[a]*Institute of Physical Chemistry, Justus-Liebig-University Giessen, Heinrich-Buff-Ring 17, D-35392 Giessen, Germany.*

[b]*Center for Materials Research (LaMa), Justus-Liebig-University Giessen, Heinrich-Buff-Ring 16, D-35392 Giessen, Germany.*

Abstract

The sodium-ion conducting family of Na$_3$PnS$_4$, with Pn = P, Sb, have gained interest for the use in solid-state batteries due to their high ionic conductivity. However, significant improvements to the conductivity have been hampered by the lack of aliovalent dopants that can introduce vacancies into the structure. Inspired by the need for vacancy introduction into Na$_3$PnS$_4$, the solid solutions with WS$_4^{2-}$ introduction are explored. The influence of the substitution with WS$_4^{2-}$ for PS$_4^{3-}$ and SbS$_4^{3-}$, respectively, is monitored using a combination of X-ray diffraction, Raman and impedance spectroscopy. With increasing vacancy concentration improvements resulting in a very high ionic conductivity of 13 ± 3 mS·cm^{-1} for Na$_{2.9}$P$_{0.9}$W$_{0.1}$S$_4$ and 41 ± 8 mS·cm^{-1} for Na$_{2.9}$Sb$_{0.9}$W$_{0.1}$S$_4$ can be observed. This work acts as a stepping-stone towards further engineering of ionic conductors using vacancy-injection via aliovalent substituents.

TOC Graphic
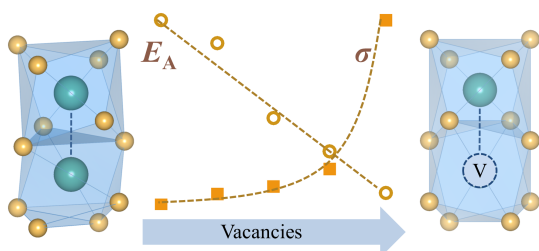
Lithium and sodium thiophosphates are currently of high interest for solid-state battery applications due to their high ionic conductivity and ductile nature. A multitude of structural classes such as $Li_{10}(Si/Ge/Sn)P_2S_{12}$,[1–9] Li_6PS_5X[10–15] in the case of Li^+ conductors and $Na_{11}Sn_2PS_{12}$,[16–18] Na_3PS_4 and Na_3SbS_4 for Na^+ conductors have attracted quite some interest.[19–24] However, while most of these compounds possess vacant sites for the mobile carrier within the structure, a prerequisite for fast ionic conduction,[25,26] Na_3PS_4 and Na_3SbS_4 are intrinsically hindered by fully occupied Na^+ positions.

The structure of Na_3PnS_4, with Pn = P, Sb, is displayed in Figure 1, crystallizing either in the cubic $I\bar{4}3m$ or tetragonal $P\bar{4}2_1c$ space groups. The cubic polymorph features a body centered cubic arrangement of the PnS_4^{3-} units, whereas the tetragonal polymorph exhibits a rotation of PnS_4^{3-} around the [111] axis that goes along with a minor tetragonal distortion along the c-axis. In the cubic structure, only one fully occupied Na^+ position exists, while in the tetragonal structure, two Na^+ positions can be found due to this tetragonal distortion resulting from the PnS_4^{3-} rotation.[22,27] The resulting, fully occupied Na^+ diffusion pathways are illustrated in Figure 1.

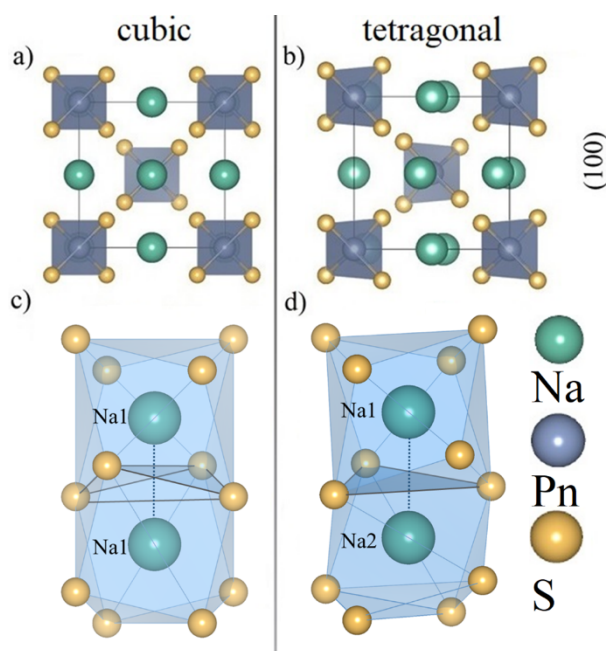Figure 1. Unit cells of the (a) cubic and (b) tetragonal Na_3PnS_4 with Pn = P, Sb. A full Na^+ occupancy within the direct diffusion pathway can be found in both the (c) cubic and (d) tetragonal polymorphs.

Different isoelectronic substitutions, such as Se for S and Sb for P, have already been carried out toward improving our understanding of this material system.[27–29] Substituting Se into the anion sublattice is possible over the whole stoichiometric range, leading to a stabilization of the

cubic polymorph and general expansion of the lattice.[27,30] This Se substitution also leads to a lattice softening, which in turn decreases both the activation energy for ion migration and the Arrhenius prefactor.[27,31] Interestingly, further improvement of the conductivity up to 0.74 mS·cm^{-1} can be achieved by mixing Na_3PS_4 with small amounts of Na_4SiS_4, highlighting the potential of this material class.[32] Furthermore, depending on the synthetic conditions, it is also possible to individually synthesize the cubic and tetragonal polymorphs. For example, while mechanical alloying leads to the cubic polymorph, the tetragonal structure can be obtained by classic high temperature synthesis.[19,24,33] Compared to Na_3PS_4, Na_3SbS_4 exhibits an even higher ionic conductivity due to the overall lower activation barriers found in both polymorphs.[33] In line with the full occupancy of the Na^+ positions, the transport properties seem to depend on the defect concentration and thus, the synthesis conditions, and less on the crystal structure itself.[22,34] This assumption is further affirmed upon considering the exceptionally high conductivity of 3 mS·cm^{-1} of the ball-milled t-Na_3SbS_4 (with 2.5 mol % Na vacancies).[29]

The existence of the fully occupied positions of Na^+ are the reason that has made it difficult to optimize the ionic conductivity. The typical aliovalent dopants within the PS_4^{3-} and SbS_4^{3-} units are often tetravalent such as Si^{4+}, Ge^{4+}, Sn^{4+}.[35] However, while these dopants work well in systems with a high number of vacant sites, they introduce more Na^+ as mobile carries and hence cannot be incorporated in the structures of Na_3PS_4 and Na_3SbS_4. While vacancy-injection via substitution of S^{2-} with Cl^- and Na^+ with Ca^{2+} has been proposed,[36,37] no substitution on the MS_4^{3-} tetrahedral center was shown until recently.[38] Thus, inspired by the need to create more vacancies in Na_3PS_4 and Na_3SbS_4, this work explores aliovalent substitutions within $Na_{3-x}Pn_{1-x}W_xS_4$. Incorporation of W^{6+} on the tetrahedral site, forming WS_4^{2-} tetrahedra, leads to the introduction of vacancies via charge compensation. It should be noted that, in addition to the substitution with W^{6+}, the substitution of Na_3PnS_4 with Mo^{6+} was attempted but synthetically unsuccessful.
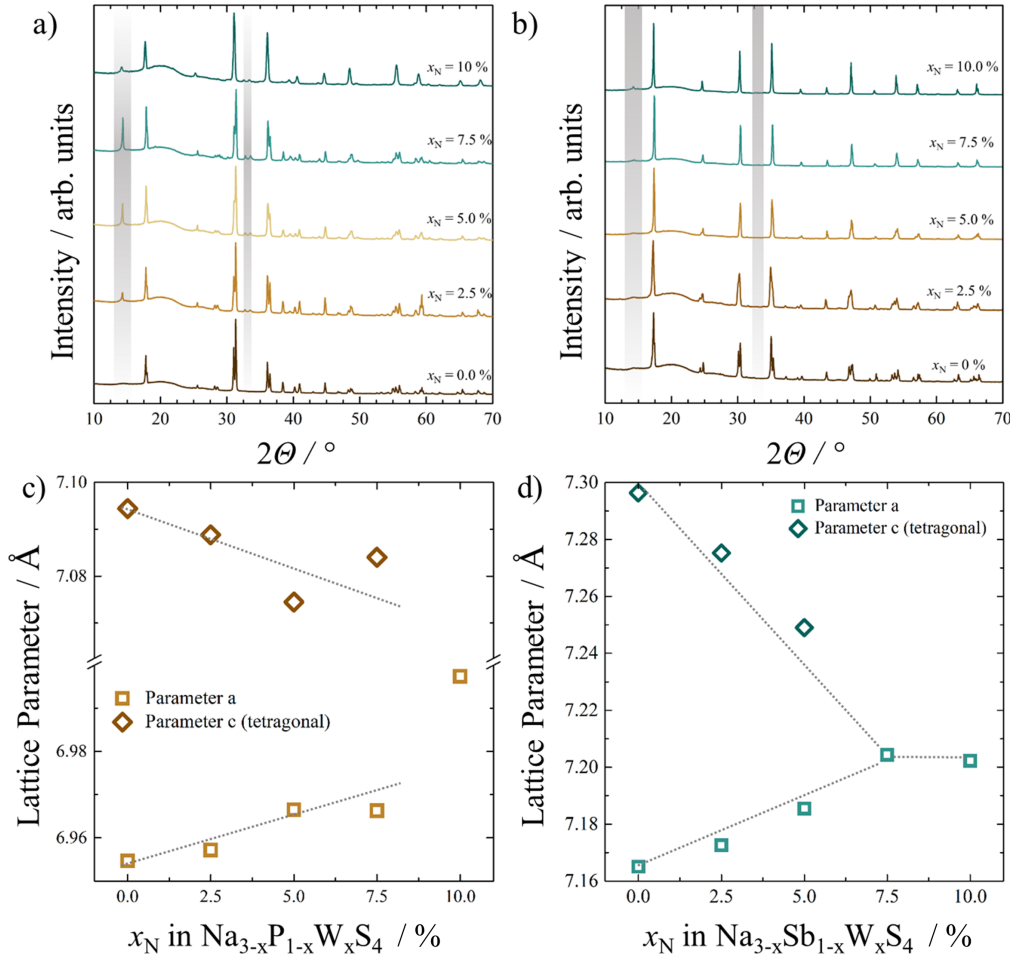
Figure 2. Obtained X-ray diffraction patterns of (a) $Na_{3-x}P_{1-x}W_xS_4$ and (b) $Na_{3-x}Sb_{1-x}W_xS_4$ with changing W content. The grey bars highlight the reflections of WS_2. Refined lattice parameters of (c) $Na_{3-x}P_{1-x}W_xSb_4$ and (d) $Na_{3-x}Sb_{1-x}W_xS_4$, showing the structural changes during substitution. In both solid solutions, changes in the lattice parameters can be found during subsitution, leading to a decrease in the tetragonal distortion (c/a ratio) and ultimately a transition from the tetragonal into the cubic crystal structure.

All experimental details on the solid-state syntheses and characterization can be found in the Supporting Information. Figures 2 a,b show the X-ray diffraction patterns of $Na_{3-x}Pn_{1-x}W_xS_4$ from $0 \leq x \leq 0.1$. Rietveld refinements of the laboratory X-ray diffraction data were performed, but deemed unreliable due to unphysically large thermal displacement parameters of Na^+ of $>$ 10 $Å^2$. While these large displacement parameters serve as an indicator for fast ionic conduction, an accurate refinement of atomic positions and occupancies becomes impossible within the whole solid solution, underlining the need for high-resolution scattering experiments. Nevertheless, the lattice parameters obtained with Pawley refinements of the solid solutions $Na_{3-x}P_{1-x}W_xS_4$ and $Na_{3-x}Sb_{1-x}W_xS_4$ can be found in Figure 2c and 2d, respectively. All Pawley fits to the diffraction data, as well as a table containing the refined lattice parameters, can be

found in the Supporting Information. With increasing W content, interesting changes in the patterns and the lattice of $Na_{3-x}P_{1-x}W_xS_4$ and $Na_{3-x}Sb_{1-x}W_xS_4$ can be observed:

(1) A certain phase fraction of the precursor WS_2 can be found in all samples of W substituted $Na_{3-x}P_{1-x}W_xS_4$ and above $x > 0.075$ minor reflections of WS_2 can also be seen in $Na_{3-x}Sb_{1-x}W_xS_4$. As WS_2 is isotypic with the MoS_2 layered structure, all of these reflections are likely influenced by texturing of a minor impurity precursor phase fraction or suggest a limited solubility in the structure of $Na_{3-x}P_{1-x}W_xS_4$. It is therefore difficult to assess the real solubility limit in the structure, based on these phase fractions.

(2) However, a systematic shift of the lattice parameters can be found during the WS_4^{2-} incorporation. With increasing W-content in $Na_{3-x}Pn_{1-x}W_xS_4$ the lattice parameter a increases while the lattice parameter c decreases and an overall decrease of the tetragonal distortion can be found. The changes in the lattice parameters and lattice volume (see Supporting Information Figure S3) are small for $Na_{3-x}P_{1-x}W_xS_4$, indicating a rather limited solubility when compared to $Na_{3-x}Sb_{1-x}W_xS_4$, as a much stronger trend can be found for $Na_{3-x}Sb_{1-x}W_xS_4$. The solubility limit seems to have been reached above $x \geq 0.1$ within $Na_{3-x}Sb_{1-x}W_xS_4$. This is further supported by the changing unit cell volume of $Na_{3-x}Sb_{1-x}W_xS_4$, which remains constant for $x = 0.1$ and 0.125, as shown in the Supporting Information Figure S5.

At this point, the differences in the changing lattice between the solid solutions $Na_{3-x}P_{1-x}W_xS_4$ and $Na_{3-x}Sb_{1-x}W_xS_4$ remain unclear as the tetrahedrally-coordinated ionic radius difference between Sb^{5+} vs. W^{6+} is low, whereas P^{5+} exhibits a much smaller ionic radius.[39] The differences are likely due to different solubility limits of WS_2 in the phases. In addition, competing effects during the introduction of Na^+ vacancies may lead to an overall lattice volume contraction (see Supporting Information Figure S5) and changing tetrahedral distortion.

(3) In both solid solutions, the decreasing tetragonal distortion leads to a structural change from the tetragonal to the cubic polymorph around $x = 0.1$ and $x = 0.075$ in $Na_{3-x}P_{1-x}W_xS_4$ and $Na_{3-x}Sb_{1-x}W_xS_4$, respectively.

(4) Ultimately, while low-temperature X-ray diffraction will be needed to assess an accurate vacancy concentration and the possibility of altered diffusion pathways and behavior, a refinement of the W-occupancy in $Na_{2.9}Sb_{0.9}W_{0.1}S_4$ was possible using synchrotron X-ray diffraction. A Rietveld refinement of the sample with the highest W-content against the higher resolution data can be found in the Supporting Information, Figure S6. The refinement provides a W-occupancy of $11.0(4)$ % and with it a high Na^+ vacancy concentration.

These structural data suggest that the introduction of W^{6+} in Na$_{3-x}$Pn$_{1-x}$W$_x$S$_4$ is possible. In addition, Raman spectroscopy is quite reliable in detecting the local polyhedral species in thiophosphates,[31,40] and can be used to monitor the generation of WS$_4^{2-}$ tetrahedra within the structure. The Raman spectra of Na$_{3-x}$P$_{1-x}$W$_x$S$_4$ and Na$_{3-x}$Sb$_{1-x}$W$_x$S$_4$, are shown in Figure 3a and 3b, respectively. For comparison, representative Raman spectra of solid WS$_2$ and the WS$_4^{2-}$ ion in solution are shown.[41–43]

In the case of Na$_{3-x}$P$_{1-x}$W$_x$S$_4$, all Raman modes of the PS$_4^{3-}$ can be found, along with the main symmetric A_1 stretching mode at 413 cm^{-1}.[31] In the Raman spectra of Na$_{3-x}$Sb$_{1-x}$W$_x$S$_4$, three Raman signals can be noticed in the range of 340 cm^{-1} to around 410 cm^{-1} corresponding to the different modes of the SbS$_4^{3-}$ tetrahedra in Na$_3$SbS$_4$.[44,45] With increasing W-content, the intensity of the main modes decrease and additional Raman active modes can be found. Additionally, a different signal around 470 cm^{-1} begins to evolve, corresponding to the vibrations of the WS$_4^{2-}$ tetrahedra (shown in grey). A minor intensity corresponding to the WS$_2$ precursor can be found in the solid solution Na$_{3-x}$P$_{1-x}$W$_x$S$_4$, indicating a different and lower solubility limit of WS$_4^{2-}$ in Na$_{3-x}$P$_{1-x}$W$_x$S$_4$ compared to Na$_{3-x}$Sb$_{1-x}$W$_x$S$_4$. The assignment of all Raman modes for PS$_4^{3-}$, SbS$_4^{3-}$, WS$_2$ and WS$_4^{2-}$ can be found in the Supporting Information, Table S3 as well as all Raman spectra including $x = 0.025$ and $x = 0.075$ in Figure S6. While minor shifts and differences in intensity are expected due to the reference spectrum stemming from thiometallocomplexes in solution, comparison of the reference spectra with the data corroborate the incorporation of WS$_4^{2-}$ tetrahedra in Na$_{3-x}$Sb$_{1-x}$W$_x$S$_4$, as well as Na$_{3-x}$P$_{1-x}$W$_x$S$_4$ to a minor extent.
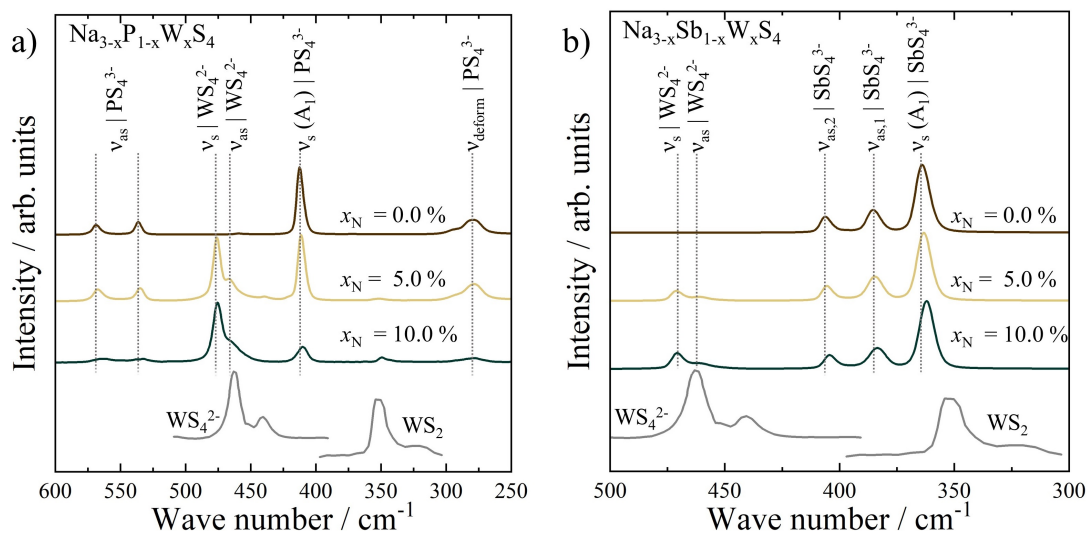

Figure 3. Raman spectra of (a) Na$_{3-x}$P$_{1-x}$W$_x$Sb$_4$ and (b) Na$_{3-x}$Sb$_{1-x}$W$_x$S$_4$ for representative compositions, along with digitized Raman spectra of WS$_4^{2-}$ polyhedra in solution,[41,42] and single

crystalline WS$_2$.[43] *In both cases, the Raman modes of the WS$_4^{2-}$ polyhedra are visible and increase with increasing degree of substitution. In addition, WS$_2$ can be found in the compositional series of Na$_{3-x}$P$_{1-x}$W$_x$Sb$_4$.*

In order to gain insight into how the increasing defect concentration by Na$^+$ vacancies affect the ionic transport properties, AC impedance spectroscopy was performed on Na$_{3-x}$Pn$_{1-x}$W$_x$S$_4$. Representative Nyquist-plots of the impedance response at -20 °C are shown for all compositions in the Supporting Information, Figure S7. In the more resistive samples of Na$_3$PS$_4$ and Na$_3$SbS$_4$, two semicircles can be found and the bulk and grain boundary contributions can be fully distinguished. However, in all other samples, only one process is visible followed by the blocking electrode. While the capacitances of the resolvable spectra are in the range of 38–64 pF·cm^{-2} for the high-frequency process, corroborating that predominantly bulk transport is observed,[46] the bulk and grain processes of the highly conducting compositions cannot be distinguished. Therefore, all ionic conductivities and activation barriers presented here need to be considered as total conductivities.

The Arrhenius plots of all compositions can be found in Figure S7. It should be mentioned that for Na$_{3-x}$Sb$_{1-x}$W$_x$S$_4$ with x = 0.05 and x = 0.075, a change in the Arrhenius behavior can be observed at temperatures slightly above room temperature (see Supporting Information, Figure S8). Typically, the cubic structure is the high-temperature polymorph. In Na$_3$SbS$_4$, one would expect the phase transition from the tetragonal to the cubic structure at 170 °C.[33] Considering the Arrhenius behavior during heating, as well as the structural changes in Figure 2, it seems that the W substitution not only lowers the tetragonal distortion in the structure, but also the phase transition temperature, similar to Na$_3$PS$_{4-x}$Se$_x$.[27] Therefore, with increasing W content, the phase transition temperature seems to decrease. For x < 0.05, the phase transition is likely located above room temperature, whereas at x ≥ 0.075, the cubic phase seems to be the stable polymorph at room temperature.

Figure 4 shows the ionic conductivity and activation barriers for Na$_{3-x}$Pn$_{1-x}$W$_x$S$_4$. With increasing W content, and with-it increasing vacancy concentration, the activation barriers for ionic transport decrease in both series of compositions. While the structural data suggests a low solubility of W^{6+} in Na$_{3-x}$P$_{1-x}$W$_x$S$_4$, the Raman data show the incorporation of WS$_4^{2-}$ and the transport properties are affected. The incorporation of W^{4+} can be ruled out as a d^2 electronic system would not exist in a tetrahedral symmetry as seen in the Raman and it would further increase the electronic conductivity. In order to assess if the incorporation of WS$_4^{2-}$ increases the electronic conductivity, DC polarization was exemplarily performed on Na$_{2.9}$Sb$_{0.9}$W$_{0.1}$S$_4$

and the results are shown in Figure S9. An electronic conductivity of $3.4 \pm 0.4 \cdot 10^{-6}$ mS·cm^{-1} shows a negligible electronic conductivity that is seven orders of magnitude lower than the ionic conductivity.

As the overall lattice volume within the solid solution is decreasing, the decreasing activation barriers are likely related to changing defect formation enthalpies due to the incorporation of vacancies, rather than changing widths of the diffusion pathways. Theoretical work also suggests that incorporation of vacancies should lead to lower activation barriers.[34] With these changes in the activation barriers and the changing carrier densities from the vacancy-injection, the ionic conductivity of both series increases significantly. While the W-substituted samples immediately exhibit a sharp increase of the conductivity and then a steadily rising conductivity with increasing W-content, the solid solution $Na_{3-x}P_{1-x}W_xS_4$ shows a much steeper jump at the tetragonal to cubic transition. As previously mentioned, the values presented here represent total conductivities and, especially in the pristine compositions, a large grain boundary contribution can be observed. The larger grain resistance is likely due to the differences in the synthetic procedure when compared to literature. Nevertheless, in the case of $Na_{3-x}P_{1-x}W_xS_4$, the unsubstituted compound exhibits a total conductivity of 0.04 ± 0.01 mS·cm^{-1} and achieves 13 ± 3 mS·cm^{-1} for $x = 0.1$, representing an increase of the conductivity exceeding three orders of magnitude. In the case of $Na_{3-x}Sb_{1-x}W_xS_4$, the pristine compound exhibits a conductivity of 0.01 ± 0.002 mS·cm^{-1} and achieves 41 ± 8 mS·cm^{-1} for $x = 0.1$. To the best of our knowledge, this is the highest ionic conductivity measured in the class of thiophosphate ionic conductors to date, showing the drastic influence of vacancy injection in $Na_{3-x}Pn_{1-x}W_xS_4$.
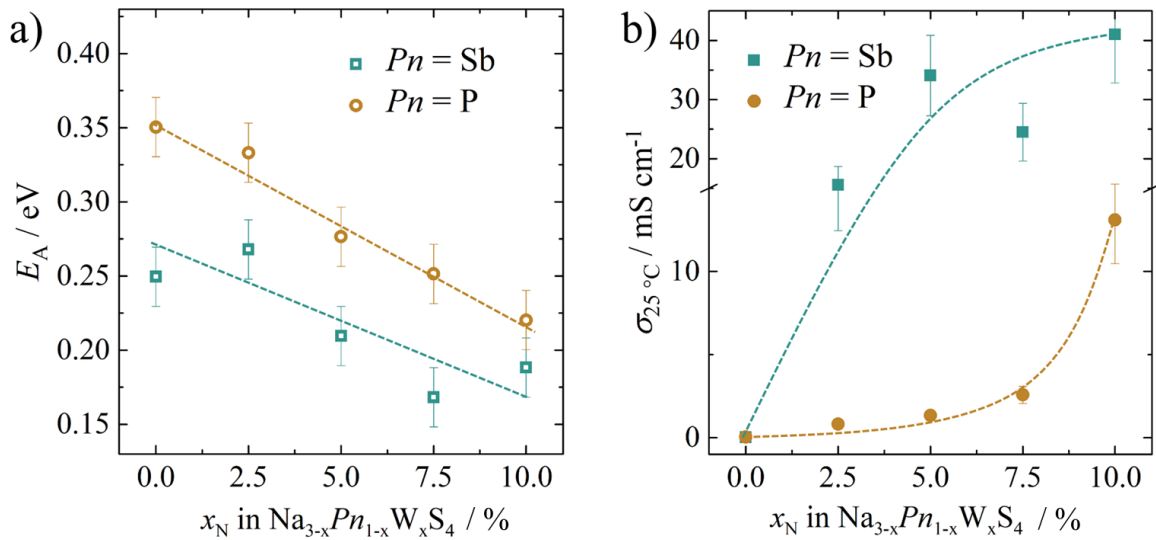
Figure 4. (a) Activation barriers of Na$_{3-x}$Pn$_{1-x}$W$_x$S$_4$ with Pn = P, Sb. and (b) room-temperature conductivities With increasing vacancy content, the conductivity changes drastically alongside with a continuous decrease of the activation barrier. Dashed lines represent guides-to-the-eye.

In conclusion, this work reports the aliovalent substitution in the solid solution series Na$_{3-x}$*Pn*$_{1-x}$W$_x$S$_4$ with *Pn* = P and Sb. X-ray diffraction and Raman spectroscopy corroborate that solid solutions can be formed and that WS$_4^{2-}$ polyhedra are incorporated into the structure. With increasing W content, the structures become less distorted leading to a structural transition from the tetragonal to the cubic phase. The increasing vacancy concentration leads to orders of magnitude improvements in the ionic conductivity, exhibiting a very high ionic conductivity of 13 ± 3 mS·cm^{-1} for Na$_{2.9}$P$_{0.9}$W$_{0.1}$S$_4$ and 41 ± 8 mS·cm^{-1} for Na$_{2.9}$Sb$_{0.9}$W$_{0.1}$S$_4$.

Future work needs to further explore the structural changes and occupancies during the substitution using low-temperature, high-resolution diffraction methods, as well as elucidating the real defect concentration and changing phase transition temperatures. Further, an assessment of the influence of the W substitution on the electrochemical stability window and the applicability in a solid-state battery is needed. Overall, this work shows that aliovalent substitutions toward increasing vacancy content is possible by introducing WS$_4^{2-}$ in the thiophosphates and thioantimonates, thereby opening up a new and very promising route for optimization of these classes of superionic conductors, beyond Na$_3$PS$_4$ and Na$_3$SbS$_4$.

Supporting Information.

All experimental details on synthesis, X-ray diffraction and impedance spectroscopy can be found here. All structural data as obtained from Pawley refinements can be found here. In addition, assignments of the Raman modes and all Raman spectra are given. Further, the impedance data and Arrhenius plot, as well as information on the Arrhenius behavior and phase transitions. Further, a Rietveld refinement against synchrotron data and DC polarization measurements of Na$_{2.9}$Sb$_{0.9}$W$_{0.1}$S$_4$ can be found.

AUTHOR INFORMATION

Corresponding Author

*wolfgang.g.zeier@pc.jlug.de;

Notes

The authors declare no competing financial interests.

Acknowledgements

References

(1)   Kamaya, N.; Homma, K.; Yamakawa, Y.; Hirayama, M.; Kanno, R.; Yonemura, M.; Kamiyama, T.; Kato, Y.; Hama, S.; Kawamoto, K.; Mitsui, A. A Lithium Superionic Conductor. *Nat. Mater.* **2011**, *10*, 682–686.

(2)   Hori, S.; Taminato, S.; Suzuki, K.; Hirayama, M.; Kato, Y.; Kanno, R. Structure–Property Relationships in Lithium Superionic Conductors Having a $Li_{10}GeP_2S_{12}$ -Type Structure. *Acta Cryst. B Eng. Mater.* **2015**, *71*, 727–736.

(3)   Kwon, O.; Hirayama, M.; Suzuki, K.; Kato, Y.; Saito, T.; Yonemura, M.; Kamiyama, T.; Kanno, R. Synthesis, Structure, and Conduction Mechanism of the Lithium Superionic Conductor $Li_{10+\delta}Ge_{1+\delta}P_{2-\delta}S_{12}$. *J. Mater. Chem. A* **2015**, *3*, 438–446.

(4)   Kato, Y.; Hori, S.; Saito, T.; Suzuki, K.; Hirayama, M.; Mitsui, A.; Yonemura, M.; Iba, H.; Kanno, R. High-Power All-Solid-State Batteries Using Sulfide Superionic Conductors. *Nat. Energy* **2016**, 16030.

(5)   Krauskopf, T.; Culver, S. P.; Zeier, W. G. The Bottleneck of Diffusion and Inductive Effects in $Li_{10}Ge_{1-X}Sn_xP_2S_{12}$. *Chem. Mater.* **2018**, *30*, 1791–1798.

(6)   Bron, P.; Johansson, S.; Zick, K.; Schmedt auf der Günne, J.; Dehnen, S.; Roling, B. $Li_{10}SnP_2S_{12}$: An Affordable Lithium Superionic Conductor. *J. Am. Chem. Soc.* **2013**, *135*, 15694–15697.

(7)   Kuhn, A.; Duppel, V.; Lotsch, B. V. Tetragonal $Li_{10}GeP_2S_{12}$ and Li_7GePS_8 – Exploring the Li Ion Dynamics in LGPS Li Electrolytes. *Energy Environ. Sci.* **2013**, *6*, 3548–3552.

(8)   Kuhn, A.; Gerbig, O.; Zhu, C.; Falkenberg, F.; Maier, J.; Lotsch, B. V. A New Ultrafast Superionic Li-Conductor: Ion Dynamics in $Li_{11}Si_2PS_{12}$ and Comparison with Other Tetragonal LGPS-Type Electrolytes. *Phys. Chem. Chem. Phys.* **2014**, *16*, 14669–14674.

(9)   Harm, S.; Hatz, A.; Moudrakovski, I.; Eger, R.; Kuhn, A.; Hoch, C.; Lotsch, B. V. Lesson Learned from NMR: Characterization and Ionic Conductivity of LGPS-like Li_7SiPS_8. *Chem. Mater.* **2019**, *31*, 1280–1288.

(10)   Ohno, S.; Helm, B.; Fuchs, T.; Dewald, G.; Kraft, M.; Culver, S.; Senyshyn, A.; Zeier, W. Further Evidence for Energy Landscape Flattening in the Superionic Argyrodites $Li_{6+x}P_{1-x}M_xS_5I$ (M = Si, Ge, Sn). *Chem. Mater.* **2019**, *31*, 4936–4944.

(11)   Deiseroth, H. J.; Kong, S. T.; Eckert, H.; Vannahme, J.; Reiner, C.; Zaiß, T.; Schlosser, M. Li_6PS_5X: A Class of Crystalline Li-Rich Solids with an Unusually High Li+ Mobility. *Angew. Chem. Int. Ed.* **2008**, *47*, 755–758.

(12)   Kraft, M. A.; Culver, S. P.; Calderon, M.; Böcher, F.; Krauskopf, T.; Senyshyn, A.; Dietrich, C.; Zevalkink, A.; Janek, J.; Zeier, W. G. Influence of Lattice Polarizability on the Ionic Conductivity in the Lithium Superionic Argyrodites Li_6PS_5X (X = Cl, Br, I). *J. Am. Chem. Soc.* **2017**, *139*, 10909–10918.

(13)   Kraft, M. A.; Ohno, S.; Zinkevich, T.; Koerver, R.; Culver, S. P.; Senyshyn, A.; Indris, S.; Morgan, B. J.; Zeier, W. G. Inducing High Ionic Conductivity in the Lithium Superionic Argyrodites $Li_{6+x}P_{1-x}Ge_xS_5I$ for All-Solid-State Batteries. *J. Am. Chem. Soc.* **2018**, *140*, 16330–16339.

(14)   Kong, S. T.; Deiseroth, H. J.; Reiner, C.; Gün, O.; Neumann, E.; Ritter, C.; Zahn, D. Lithium Argyrodites with Phosphorus and Arsenic : Order and Disorder Of. *Chem. Eur. J.* **2010**, *6*, 2198–2206.

(15)   De Klerk, N. J. J.; Wagemaker, M. Diffusion Mechanism of the Sodium-Ion Solid Electrolyte Na_3PS_4 and Potential Improvements of Halogen Doping. *Chem. Mater.* **2016**, *28*, 3122–3130.

(16)   Duchardt, M.; Roling, B.; Ruschewitz, U.; Adams, S.; Dehnen, S. Vacancy-Controlled Na^+ Superion Conduction in $Na_{11}Sn_2PS_{12}$. *Angew. Chem. Int. Ed.* **2018**, *57*, 1351–1355.

(17)   Duchardt, M.; Neuberger, S.; Ruschewitz, U.; Krauskopf, T.; Zeier, W. G.; Gu, D.; Adams, S.; Roling, B.; Dehnen, S. Superion Conductor $Na_{11.1}Sn_{2.1}P_{0.9}Se_{12}$: Lowering the Activation Barrier of Na+ Conduction in Quaternary 1−4−5−6 Electrolytes. *Chem. Mater.* **2018**, *30*, 4134–4139.

(18)   Zhang, Z.; Ramos, E.; Lalere, F.; Assoud, A.; Kaup, K.; Hartmann, P.; Nazar, L. $Na_{11}Sn_2PS_{12}$: A New Solid State Sodium Superionic Conductor. *Energy Environ. Sci.* **2017**, *11*, 87–93.

(19)   Jansen, M.; Henseler, U. Synthesis, Structure Determination, and Ionic Conductivity of Sodium Tetrathiophosphate. *J. Solid State Chem.* **1992**, *99*, 110–119.

(20)   Hayashi, A.; Noi, K.; Tanibata, N.; Nagao, M.; Tatsumisago, M. High Sodium Ion Conductivity of Glass-Ceramic Electrolytes with Cubic Na_3PS_4. *J. Pow. Source* **2014**, *258*, 420–423.

(21)   De Klerk, N. J. J.; Wagemaker, M. Diffusion Mechanism of the Sodium-Ion Solid Electrolyte Na_3PS_4 and Potential Improvements of Halogen Doping. *Chem. Mater.* **2016**, *28*, 3122–3130.

(22)   Krauskopf, T.; Culver, S. P.; Zeier, W. G. Local Tetragonal Structure of the Cubic Superionic Conductor Na_33PS_4. *Inorg. Chem.* **2018**, *57*, 4739–4744.

(23) Zhu, Z.; Chu, I. H.; Deng, Z.; Ong, S. P. Role of Na^+ Interstitials and Dopants in Enhancing the Na^+ Conductivity of the Cubic Na_3PS_4 Superionic Conductor. *Chem. Mater.* **2015**, *27*, 8318–8325.

(24) Hayashi, A.; Noi, K.; Sakuda, A.; Tatsumisago, M. Superionic Glass-Ceramic Electrolytes for Room-Temperature Rechargeable Sodium Batteries. *Nat. Commun.* **2012**, *3*, 856.

(25) Wang, Y.; Richards, W. D.; Ong, S. P.; Miara, L. J.; Kim, J. C.; Mo, Y.; Ceder, G. Design Principles for Solid-State Lithium Superionic Conductors. *Nat. Mater.* **2015**, *14*, 1026–1031.

(26) Culver, S. P.; Krauskopf, T.; Koerver, R.; Zeier, W. G. Designing Ionic Conductors: The Interplay between Structural Phenomena and Interfaces in Thiophosphatebased Solid-State Batteries. *Chem. Mater.* **2018**, *30*, 4179–4192.

(27) Krauskopf, T.; Pompe, C.; Kraft, M.; Zeier, W. G. Influence of Lattice Dynamics on Na^+-Transport in the Solid Electrolyte $Na_3PS_{4-x}Se_x$. *Chem. Mater.* **2017**, *29*, 8859–8869.

(28) Zhang, L.; Yang, K.; Mi, J.; Lu, L.; Zhao, L.; Wang, L.; Li, Y.; Zeng, H. Na_3PSe_4: A Novel Chalcogenide Solid Electrolyte with High Ionic Conductivity. *Adv. Energy Mater.* **2015**, 1501294.

(29) Zhang, L.; Zhang, D.; Yang, K.; Yan, X.; Wang, L.; Mi, J.; Xu, B.; Li, Y. Vacancy-Contained Tetragonal Na_3SbS_4 Superionic Conductor. *Adv. Sci.* **2016**, *3*, 1600089.

(30) Xiong, S.; Liu, Z.; Rong, H.; Wang, H.; Mcdaniel, M.; Chen, H. $Na_3SbSe_{4-x}S_x$ as Sodium Superionic Conductors. *Sci. Rep.* **2018**, *8*, 9146.

(31) Krauskopf, T.; Muy, S.; Culver, S. P.; Ohno, S.; Delaire, O.; Shao-Horn, Y.; Zeier, W. G. Comparing the Descriptors for Investigating the Influence of Lattice Dynamics on Ionic Transport Using the Superionic Conductor $Na_3PS_{4-x}Se_x$. *J. Am. Chem. Soc.* **2018**, *140*, 14464–14473.

(32) Tanibata, N.; Noi, K.; Hayashi, A.; Tatsumisago, M. Preparation and Characterization of Highly Sodium Ion Conducting Na_3PS_4–Na_4SiS_4 Solid Electrolytes. *RSC Adv.* **2014**, *4*, 17120–17123.

(33) Zhang, D.; Cao, X.; Xu, D.; Wang, N.; Yu, C.; Hu, W.; Yan, X.; Mi, J.; Wen, B.; Wang, L.; Zhang, L. Synthesis of Cubic Na_3SbS_4 Solid Electrolyte with Enhanced Ion Transport for All-Solid-State Sodium-Ion Batteries. *Electrochim. Acta* **2018**, *259*, 100–109.

(34) Bo, S. H.; Wang, Y.; Kim, J. C.; Richards, W. D.; Ceder, G. Computational and

Experimental Investigations of Na-Ion Conduction in Cubic Na_3PSe_4. *Chem. Mater.* **2016**, *28*, 252–258.

(35)   Rao, R. P.; Chen, H.; Wong, L. L.; Adams, S. $Na_{3+x}M_xP_{1-x}S_4$ (M = $Ge^{4+}, Ti^{4+}, Sn^{4+}$) Enables High Rate All-Solid-State Na-Ion Batteries $Na_{2+2d}Fe_{2-d}(SO_4)_3|Na_{3+x}M_xP_{1-x}S_4|Na_2Ti_3O_7$. *J. Mater. Chem. A* **2017**, 3377–3388.

(36)   Chu, I. H.; Kompella, C. S.; Nguyen, H.; Zhu, Z.; Hy, S.; Deng, Z.; Meng, Y. S.; Ong, S. P. Room-Temperature All-Solid-State Rechargeable Sodium-Ion Batteries with a Cl-Doped Na_3PS_4 Superionic Conductor. *Sci. Rep.* **2016**, *6*, 33733.

(37)   Yang, H.; Kim, M.; Hong, S.; Lee, J. H.; Jung, Y. S. Vacancy-Driven Na^+ Superionic Conduction in New Ca-Doped Na_3PS_4 for All-Solid-State Na-Ion Batteries. *ACS Energy Lett.* **2018**, *3*, 2504–2512.

(38)   Hayashi, A.; Masuzawa, N.; Yubuchi, S.; Tsuji, F.; Hotehama, C.; Sakuda, A.; Tatsumisago, M. A Sodium-Ion Sulfide Solid Electrolyte with Unprecedented Conductivity at Room Temperature. *Nat. Commun.* **2019**, *10* (5266).

(39)   Shannon, R. D.; Prewitt, C. T. Revised Values of Effective Ionic Radii. *Acta Crystallogr. Sect. B Struct. Crystallogr. Cryst. Chem.* **2002**, *26*, 1046–1048.

(40)   Dietrich, C.; Weber, D. A.; Sedlmaier, S. J.; Indris, S.; Culver, S. P.; Walter, D.; Janek, J.; Zeier, W. G. Lithium Ion Conductivity in $Li_2S – P_2S_5$ Glasses –. *J. Mater. Chem. A* **2017**, *5*, 18111–18119.

(41)   Müller, A.; Jaegermann, W.; Hellmann, W. Schwingungsspektren Und Strukturchemie von Heterometall-Komplexen Und -Clustern Mit Thiometallat-Liganden. *J. Mol. Struct.* **1983**, *100*, 559–570.

(42)   Müller, A.; Hellmann, W. Electron Delocalization in Thiometallato Complexes and Clusters with Different $M'S_2MS_2$ (M' = Fe, Ag; M = Mo, W) Units Studied by Means of Resonance-Raman Spectroscopy. *Spectrochim. Acta Part A Mol. Spectrosc.* **1985**, *41*, 359–366.

(43)   Wang, F.; Kinloch, I. A.; Wolverson, D.; Tenne, R.; Zak, A.; O'Connell, E.; Bangert, U.; Young, R. J. Strain-Induced Phonon Shifts in Tungsten Disulfide Nanoplatelets and Nanotubes. *2D Mater.* **2017**, *4*, 015007.

(44)   Banerjee, A.; Park, K. H.; Heo, J. W.; Nam, Y. J.; Moon, C. K.; Oh, S. M.; Hong, S. T.; Jung, Y. S. Na_3SbS_4: A Solution Processable Sodium Superionic Conductor for All-Solid-State Sodium-Ion Batteries. *Angew. Chemie - Int. Ed.* **2016**, *55*, 9634–9638.

(45)   Mikenda, W.; Preisinger, A. Vibrational Spectra of Na_3SbS_4, $Na_3SbS_4*9H_2O$ (Schlippe's Salt) and $Na_3SbS_4*9D_2O$. *Spectrochim. Acta Part A Mol. Spectrosc.* **1980**,

36, 365–370.

(46)   Irvine, J. T. S.; Sinclair, D. C.; West, A. R. Electroceramics: Characterization by Impedance Spectroscopy. *Adv. Mater.* **1990**, *2*, 132–138.